Role of grain boundary character on oxygen and hydrogen segregation-induced embrittlement in polycrystalline Ni

Jie Chen & Avinash M. Dongare

Journal of Materials Science
Full Set - Includes `Journal of Materials Science Letters'

ISSN 0022-2461
Volume 52
Number 1

J Mater Sci (2017) 52:30-45
DOI 10.1007/s10853-016-0389-3

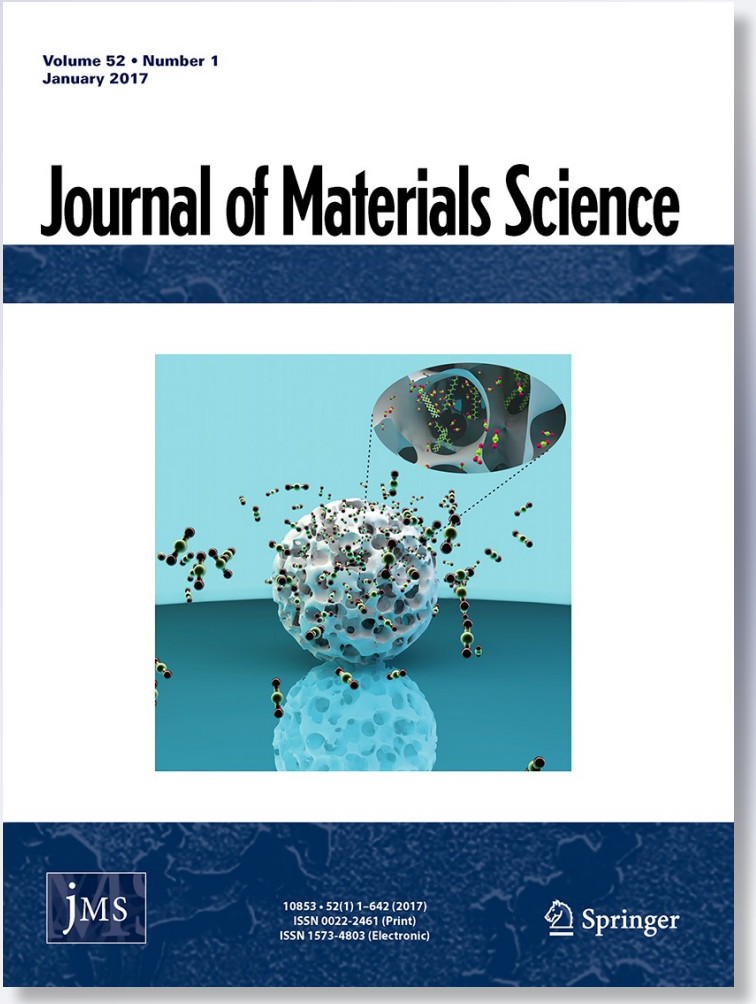

Springer

J Mater Sci (2017) 52:30–45

Role of grain boundary character on oxygen and hydrogen segregation-induced embrittlement in polycrystalline Ni

Jie Chen[1] and Avinash M. Dongare[1,*]

[1] *Department of Materials Science and Engineering, and Institute of Materials Science, University of Connecticut, Storrs, CT 06269, USA*

Received: 29 June 2016
Accepted: 7 September 2016
Published online: 21 September 2016

ABSTRACT

Density functional theory (DFT) calculations are carried out to investigate the role of grain boundaries on the energetics related to the oxygen and hydrogen segregation-induced embrittlement in polycrystalline Ni systems. Four model grain boundary (GB) systems for nickel are chosen to investigate this effect. These model GBs are the Σ5 (012) GB, the Σ5 (013) GB, the Σ11 (113) GB, and the Σ3 (111) coherent twin boundary (CTB). The chosen GBs enable the investigation of the role of the CTB in the embrittlement and decohesion mechanisms in comparison with the other GBs. The embrittling mechanism considered here is based on the investigation of the energetics related to (a) the segregation of atoms of embrittling species (oxygen, hydrogen) at the GB; (b) the formation of vacancies due to the segregation of embrittling species at the GB; and (c) the energetics related to decohesion at the GB as a function of concentration/accumulation of the embrittling species at the GB. DFT calculations suggest that the segregation of the embrittling species and the embrittling effect are closely related to the local atomic structure of the GB and the associated excess free volume. In particular, it is found that the Σ3 (111) CTB is less prone to segregation of oxygen and hydrogen based on the binding energetics of the embrittling species. However, among all the GBs considered, the Σ3 (111) CTB is found to be most susceptible to GB decohesion and crack formation in the presence of small amounts of segregated oxygen atoms. This dual behavior of the Σ3 (111) CTB is also confirmed for the case of hydrogen as the embrittling species using DFT simulations. Thus, the segregation-resistant Σ3 (111) CTB is observed to be the most susceptible to crack formation in the presence of small amounts of segregated embrittling atoms. The energetics of segregation of the embrittling species and the effect of segregation on the vacancy formation energies and GB decohesion are discussed.

Address correspondence to E-mail: dongare@uconn.edu

DOI 10.1007/s10853-016-0389-3

Introduction

Polycrystalline nickel-based superalloys, due to their high strengths and corrosion resistance, are used for components that are subjected to high stresses and temperatures in gas turbines. The combination of such loading conditions, however, results in intergranular cracking of the material at elevated temperatures [1–3]. This failure behavior is attributed to the diffusion of oxygen into the metal through the grain boundaries resulting in stress-accelerated grain boundary oxidation (SAGBO) and the failure is referred to as oxygen-induced intergranular cracking (OIC) [3–6]. As a result, several efforts have focused on the investigation of the embrittlement-induced degradation behavior of Ni and Ni-based superalloys [7–10]. The degradation behavior is attributed to a mechanism of dynamic embrittlement [11, 12], wherein a build-up of high stress concentrations is observed at the GBs followed by stress-driven diffusion of the embrittling species along the GB, which lowers the GB cohesion to nucleate a crack. Furthermore, the accumulation of the embrittling species has been reported to be more significant in the elastic field of a crack tip and thus accelerates intergranular cracking.

Thus, the embrittling mechanism is largely determined by the diffusion and preferential segregation of oxygen at the GBs which results in the formation of NiO particles [13]. The diffusion of oxygen along the grain boundaries has been attributed to the presence of vacancy sinks at the grain boundaries that act as trapping sites for the embrittling atoms at the GB. Similar to oxygen, hydrogen-induced embrittlement is also attributed to the diffusion and accumulation/trapping of hydrogen at the GBs [14–16]. For example, experiments have confirmed this effect for the Ni–H system, where GBs act as effective sinks for hydrogen trapping due to high densities of dislocations at the GBs [17]. The experiments also suggest that the presence of hydrogen atoms promotes vacancy formation along GBs via vacancy–hydrogen interaction in pure Ni. Thus, the micromechanisms for embrittlement and fracture are largely related to the energetics for segregation of the embrittling species as well as the presence/creation of vacancy sinks at the grain boundaries.

Several computational efforts have therefore focused on the energetics of segregation for various embrittling elements at the grain boundaries in Ni using atomistic simulations. These studies have investigated the energetics related to segregation of hydrogen [18, 19], boron [20], carbon [21], sulfur [22–25], bismuth [26, 27], vanadium [28], and tellurium [29] using density functional theory (DFT) and molecular dynamics (MD) simulations. Additionally, systematic studies have been devoted to explore the embrittling/strengthening potency of nonmetal sp solutes in representative Ni grain boundaries, aimed at unveiling the key factors in the effect of solute segregation on the cohesion of Ni grain boundaries [30–33]. While the segregation behavior of these embrittling species has been studied extensively, only a few of these studies have investigated the effect of impurity segregation on the decohesion behavior of the GBs, i.e., crack formation.

The process of dynamic embrittlement is also observed to be determined by the GB character, i.e., the structural environment of a GB. For example, oxygen GB diffusion is greatly reduced by an increase in the ratio of GBs with a high fraction of coincident lattice sites (CSL), i.e., *special* GBs (Σ3-Σ29) in polycrystalline Ni alloys [34]. In addition, lower Σ value (high CSL) GBs, especially Σ3 GBs, have been found to be much more resistant to intergranular oxidation than higher Σ value GBs, revealing a strong dependence of intergranular oxidation on the GB type in terms of Σ values [35]. This dependence on the structure of the GBs is likely to be attributed to the lower energy, lower oxygen diffusivity, and the high surface separation energy of the *special* GBs [36, 37]. Similar observations have been made for the case of hydrogen. For example, an increase in the ratio of *special* GBs results in a two-fold increase in tensile ductility and significantly higher fracture toughness [38]. This increase is attributed to a lower tendency for hydrogen to segregate at these *special* GBs. In addition, the Σ5 (012) GB is found to be much more effective in trapping hydrogen as compared to the close-packed Σ3 (111) CTB in Ni [39, 40]. More recent MD simulations also suggest that the presence of hydrogen leads to a decrease in the work of separation required for crack propagation (decohesion) for a Σ3 (112) GB [41]. Thus, these results suggest that improved intergranular oxidation resistance can be achieved by increasing the fraction of these *special* GBs. It can therefore be expected that a microstructure with a high density of Σ3 (111) CTBs that render enhanced

mechanical strength for the Ni-based microstructures will have higher segregation resistance for oxygen and hydrogen and in turn embrittlement. However, a recent experimental study to investigate the role of CTBs on embrittlement behavior indicated preferential nucleation of cracks at Σ3 CTBs due to hydrogen embrittlement [42]. The study speculates that the Σ3 CTBs are most susceptible to crack initiation due to hydrogen embrittlement as compared to the other grain boundaries.

Thus, a fundamental understanding of the role of the GBs and in particular the CTB on the embrittlement and crack initiation behavior is needed at the atomistic level to enhance the Ni superalloy-based component lifetimes as well as enable improvements in materials design. As a result, the links between the structural characteristics of the GBs for various model GB systems and the segregation of embrittling species (oxygen, hydrogen) as well as the segregation-induced crack formation are investigated in this paper using DFT calculations. This study uses four nickel model GB systems including the Σ3 CTB to investigate the embrittlement behavior due to segregation of oxygen and hydrogen at the GBs. The understanding of the embrittling mechanism considered here is based on the investigation of the energetics related to (a) the segregation of atoms of embrittling species (oxygen, hydrogen) at the GB; (b) the formation of vacancies due to the segregation of embrittling species at the GB (the higher concentration of vacancies promotes diffusion of the embrittling atoms to the GB and results in an increased concentration of the embrittling atoms at the GB); and (c) the energetics related to decohesion at the GB as a function of concentration of the embrittling species at the GB. While these calculations are carried out at 0 K, the computed energetics of the processes related to segregation and crack formation can provide insights into the mechanisms operating at high temperatures. However, the effects of temperature such as GB structural transformations induced by solute segregation [43–45] are ignored here.

DFT calculations are first carried out to investigate the effect of the character (structure, excess free volume) of a GB on the energetics related to segregation of embrittling species at the GBs. The effect of segregation of the embrittling species on the vacancy formation energy at sites close to the GB is then investigated for various concentrations at the GB and the potential vacancy formation sites are identified. In addition, the effect of segregation of the embrittling species on GB decohesion (crack formation) along the GB is investigated to identify the links between the GB character and embrittling response. Of particular importance is the investigation of the role of the Σ3 CTBs in the embrittlement and decohesion behavior due to segregation of oxygen and hydrogen. The paper is organized in the following way: first, computational details are presented; next the structure and energetics of the clean Ni GBs are discussed, followed by investigation of oxygen segregation energetics and decohesion effect of the Ni GBs; finally, embrittling effect of hydrogen segregation is examined.

Computational details

The four model GB systems, i.e., the Σ3 (111) GB, the Σ5 (012) GB, the Σ5 (013) GB, and the Σ11 (113) GB, are chosen for this study due to the low energies for these GBs in polycrystalline Ni [46] and or that observed experimentally [47]. It should be noted here that the Σ3 (111) GB considered here is a coherent twin boundary (CTB), unlike the other regular GBs. Each model GB system is created as a supercell containing two grains by choosing a rotation axis and a rotation angle to generate a symmetrical-tilt GB. The rotation axis and angle for the symmetrical-tilt GBs used are listed in Table 1. The supercell system is periodic in all the directions. The supercell system created therefore results in two GB planes, one in the middle and another one on the top/bottom. The side view of the various model GB systems created along the <110> zone axis for Σ3 (111) and Σ11 (113) GB, and <100> zone axis for Σ5 (012) and Σ5 (013) GB is shown in Fig. 1. The relaxed supercell dimensions are 4.94 Å × 4.73 Å × 24.26 Å for the Σ3 (111) GB, 6.80 Å × 7.82 Å × 22.91 Å for the Σ5 (012) GB,

Table 1 Structural parameters of the relaxed supercell for the model GB systems

GB	Σ3 (111)	Σ5 (012)	Σ5 (013)	Σ11 (113)
GB plane	(111)	(012)	(013)	(113)
Rotation axis	[110]	[100]	[100]	[110]
Rotation angle	109.47°	36.9°	53.1°	50.5°

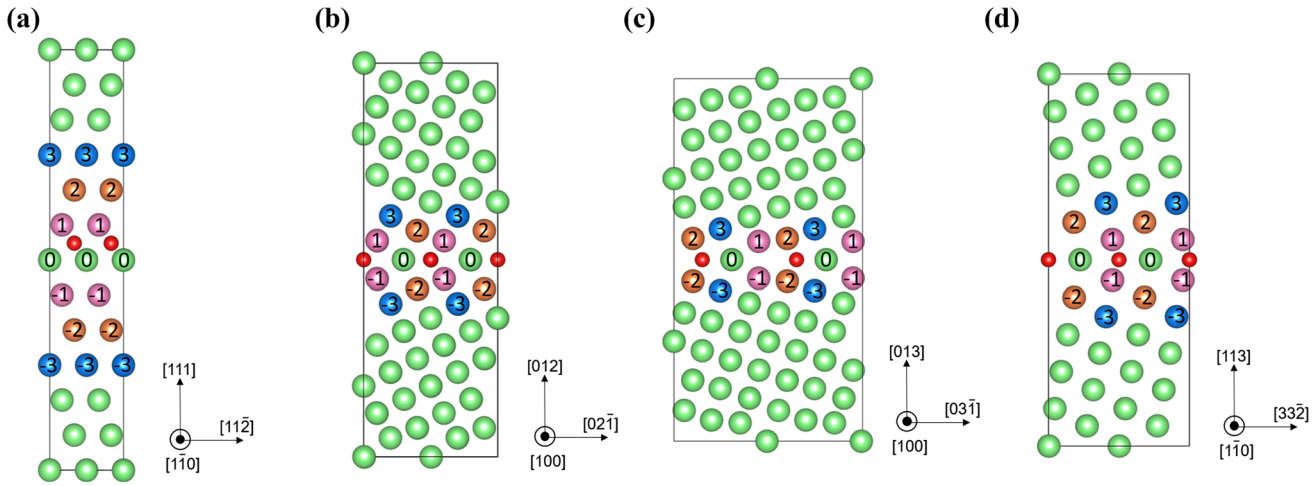

Figure 1 Supercell of model GB systems chosen viewed along <110> zone axis for **a** Σ3 (111) and **d** Σ11 (113) GB, and <100> zone axis for **b** Σ5 (012) and **c** Σ5 (013) GB. The relaxed supercell dimensions are 4.94 Å × 4.73 Å × 24.26 Å for the Σ3 (111) GB, 6.80 Å × 7.82 Å × 22.91 Å for the Σ5 (012) GB, 7.01 Å × 11.01 Å × 21.08 Å for the Σ5 (013) GB, and 4.93 Å × 8.22 Å × 21.65 Å for the Σ11 (113) GB. The grain boundary is located at the center of the superlattice and is labeled as GB_0 layer. The interstitial oxygen atom sites are also shown here and *colored red*. The layers of atoms next to the GB are labeled as GB_1, GB_2, GB_3 layer, etc., with increasing distance from the boundary layer (GB_0). The substitutional sites for layers up to GB_3 layer (colored varyingly) will be considered for oxygen, hydrogen, and vacancy segregation in this work.

7.01 Å × 11.01 Å × 21.08 Å for the Σ5 (013) GB, and 4.93 Å × 8.22 Å × 21.65 Å for the Σ11 (113) GB. The grain boundary layer of interest is in the center of the supercell and the atoms are labeled as GB_0. The layers of atoms next to the GB are labeled as GB_1, GB_2, GB_3 layer, etc., with increasing distance from the GB (as shown by the different colors of atoms). The layers up to GB_3 are colored differently and the substitutional sites in these layers are considered for vacancy formation in this work.

DFT calculations are carried out using Vienna ab initio simulation package (VASP) [48, 49], with the electronic–ion interaction described by a projector augmented wave method [50, 51] and a Perdew–Burke–Ernzerhof form generalized gradient approximation (GGA) [52] for the exchange-correlation potential. The wavefunction of a plane wave basis sets is expanded with a cutoff energy of 400 eV. The Brillouin zone integration was performed using a Monkhorst–Pack scheme [53], with a k-point mesh of 4 × 4 × 1 for Σ3 (111) GB, 3 × 3 × 1 for Σ5 (012) GB, 4 × 2 × 1 for Σ5 (013) GB, and 4 × 4 × 1 for Σ11 (113) GB. A Methfessel–Paxton smearing method is adopted, with a smearing width of 0.1 eV. Atomic positions as well as the supercell volume are allowed to relax and evolve until all forces converge to within 0.03 eV/Å. All calculations are carried out using spin polarization. A convergence test is first performed to make

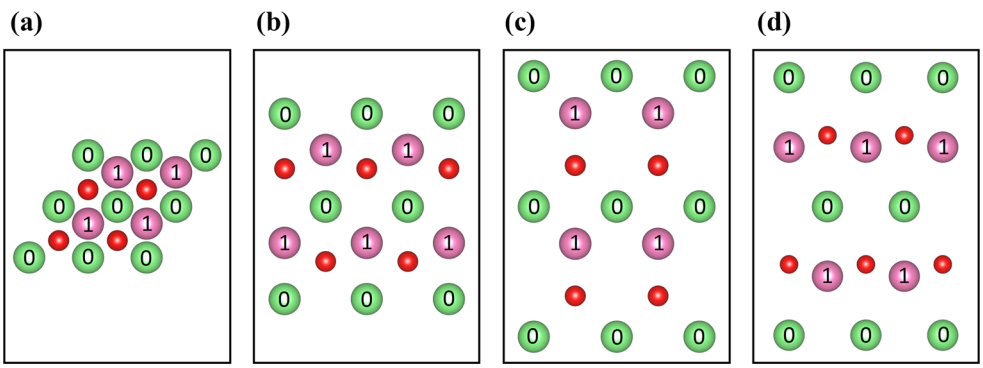

Figure 2 *Top view* (normal to GB) showing the four possible interstitial sites in GB_0 layer for the segregation of oxygen or hydrogen atoms: **a** Σ3 (111), **b** Σ5 (012), **c** Σ5 (013), and **d** Σ11 (113).

sure that the number of layers between the GBs is large enough to minimize the interaction between adjacent boundaries and represent a bulk-like simulation in the center of the grain. The interlayer spacing and GB energy are calculated for each GB and used as the convergence criteria in the determination of the supercell size needed. The supercell is validated to be large enough in the GB normal direction to accurately represent a GB when the interlayer distance at GB center reaches within 0.02 Å of the bulk value and GB energy attains a convergence of 0.03 J/m^2. Based on the results of the convergence test, 12, 28, 36, and 20 layers are found to be adequate for the Σ3 (111) GB, the Σ5 (012) GB, the Σ5 (013) GB, and the Σ11 (113) GB, respectively. A (2 × 2) cell is adopted in the GB plane for all the calculations. Each GB structure considered results in four interstitial sites for segregation of oxygen and hydrogen. These four interstitial sites are shown as small red atoms in Fig. 1 for all the GBs. The top view showing the locations of the four interstitial sites for the various model GB systems is shown in Fig. 2.

Energetics of clean GB systems and vacancy formation energy at GBs

DFT calculations are first carried out to investigate the structure and energetics of clean GB systems. The variation in the spacing between the layers at the GB and away from the GB is computed and plotted as a function of distance from the GB in Fig. 3. Specifically, for Σ5 (012) GB, the variation and magnitude in the interlayer spacing agree very well with the results reported in [31]. Such variations have also been reported for Ni Σ5 (012) GB and Fe Σ5 (013) GB [54]. An apparent oscillatory behavior is seen for all the GBs considered. While the oscillations appear large for the case of Σ3 (111) and Σ11 (113), the interlayer spacing is very close to the bulk results, and the oscillations are due to the small range of the Y-axis. These variations are very similar to the oscillatory interlayer spacing close to metal surfaces and have been shown to be a result of the redistribution of charge density at the interface [55]. Because of the mismatch of the crystal lattice at the grain boundary,

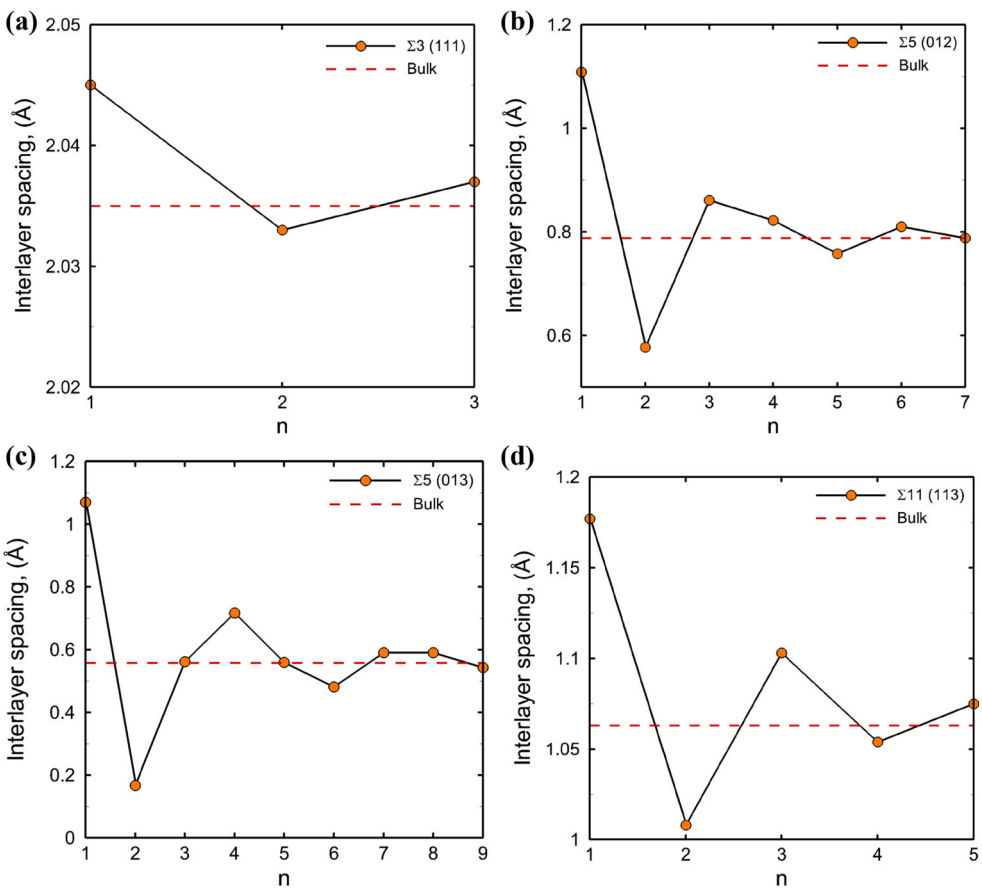

Figure 3 Calculated interlayer distance as a function of distance from the GB for the four GB systems considered: **a** Σ3 (111), **b** Σ5 (012), **c** Σ5 (013), and **d** Σ11 (113). The number n corresponds to the interlayer distance between layers $n-1$ and n. *Red dashed line* corresponds to bulk interlayer distance.

Table 2 Calculated excess free volume V_{exe} (Å) in this work and the results reported in literature and experiments

GB	Σ3 (111)	Σ5 (012)	Σ5 (013)	Σ11 (113)
V_{exe}	−0.11	0.45	0.67	0.06
MD	N/A	N/A	0.40 [57]	N/A
Experiment	0.32 ± 0.04 [53]			

atoms close to the GB occupy more volume than those arranged in a perfect single crystal. An excess free volume is therefore associated with this expansion, which is defined as the change of volume with the boundary area of a certain GB compared to that of the perfect bulk structure.

$$V_{\text{exe}} = \frac{(V_{\text{GB}} - N_{\text{GB}}\Omega)}{A} \quad (1)$$

Here, V_{GB} is the volume of the GB system, Ω is the mean atomic volume per atom in the perfect crystal, N_{GB} is the number of atoms in the GB system, and A is the boundary area. This excess free volume can be calculated experimentally [56] and has been shown to be directly related to the GB energy [57]. Additionally, this excess free volume is observed to have a profound influence over phenomena such as GB diffusion, segregation [58], and electric resistivity [59]. The calculated excess free volume for the four GBs is tabulated in Table 2 in comparison to that computed using molecular dynamics (MD) simulations [60] and that calculated experimentally [56].

The GB energy, also referred to as GB formation energy, is defined as the energy required to create a GB from bulk material per unit area. It is closely related to the mismatch of the crystal lattice at the GB and is therefore an important parameter in characterizing GBs. The GB energy is calculated as

$$\gamma_{\text{GB}} = \frac{(E_{\text{GB}} - N_{\text{GB}}\, E_{\text{atom}})}{2A}. \quad (2)$$

Here, E_{GB} is the total energy of the GB system, E_{atom} is the energy per Ni atom in the ideal FCC structure, N_{GB} is the number of atoms in the GB system, and A is the area of the grain boundary. The energy difference is divided by 2A since we have two boundary planes in the system, as mentioned before. The values for the GB energy calculated for the model GB systems are listed in Table 3 in comparison with the values reported in the literature using DFT [23, 28] and MD simulations [18, 61, 62]. It can be seen that the GB energy is observed to be the lowest for Σ3 (111) GB and highest for Σ5 (013) GB.

The energy for the formation of a vacancy is also calculated for a clean Ni bulk system and compared with those for the model GB systems. The bulk nickel system consists of 96 atoms with dimensions of 7.04 Å × 7.04 Å × 21.12 Å which is periodic in all directions. The vacancy formation energy is calculated as

$$E_f = E_{\text{tot}}^{\text{vac}} - E_{\text{tot}} + E_{\text{Ni}}. \quad (3)$$

Here, E_{tot}^{vac} is the total energy of system with a single vacancy, E_{tot} the total energy of the clean system without vacancy, and E_{Ni} the energy per Ni atom in the ideal FCC structure. The vacancy formation energy is calculated to be 1.52 eV for bulk Ni and compares well with the values of 1.77 eV calculated using other DFT calculations in the literature [63] and 1.8 eV calculated experimentally [64]. The vacancy formation energy is then calculated for the various model GB systems by considering a single vacancy at a randomly chosen site in layers GB_0, GB_1, GB_2, and GB_3. The calculated values for the vacancy formation energy at the various sites are listed in Table 4. Very little variation is observed in the vacancy formation energy for Σ3 (111) GB at the various sites chosen. For the other three GBs, GB_1 layer is found to be the most stable site. Notably, the vacancy formation energy for Σ5 (013) GB is negative at the GB_1 layer, indicating a high tendency for vacancy formation and therefore trapping of the embrittling species. The energetics for vacancy formation discussed above can also be correlated to the excess free volume at the GB. The variation of the GB energy and the vacancy formation energy are plotted in Fig. 4 as a function of the excess free volume (V_{exe}) at the GB. The plot indicates that the GB energy increases with the excess free volume

Table 3 Calculated values for GB energy (J/m^2) in comparison with the values reported in literature using DFT and MD simulations

GB	Σ3 (111)	Σ5 (012)	Σ5 (013)	Σ11 (113)
γ_{GB}	0.09	1.30	1.91	0.47
DFT	N/A	1.23 [28], 1.21 [23]	N/A	N/A
MD	0.05 [58]	1.285 [59], 1.34 [58]	1.344 [58], 1.93 [58]	0.376 [18], 0.40 [58]

Table 4 Vacancy formation energy (eV) at various sites close to GB

GB	Σ3 (111)	Σ5 (012)	Σ5 (013)	Σ11 (113)
GB_0	1.32	1.56	1.55	1.52
GB_1	1.35	0.57	−0.33	1.19
GB_2	1.38	1.30	1.06	1.43
GB_3	1.38	1.31	1.19	1.35
I_4-GB_0 + V-GB_1	−0.14	0.02	0.36	0.16
I_4-GB_0 + V-GB_2	0.57	0.82	0.88	−1.04
Bulk	1.52			

Here, V-GB_1 and V-GB_2 correspond to a single vacancy at GB_0, GB_1, GB_2 and GB_3 layers, whereas I_4-GB_0 + V-GB_1 and I_4-GB_0 + V-GB_2 correspond to vacancy formation energy at GB_1 and GB_2 layers in the presence of 4 oxygen atoms (1 ML) at GB_0 interstitial site

associated with the GB, whereas the vacancy formation energy at GB_1 layer becomes less positive, indicating more favorable vacancy formation as the excess free volume associated with the GB decreases.

The investigation of the embrittling mechanism considered here is based on the investigation of the energetics related to (a) the segregation of embrittling species at the GB; (b) the formation of vacancies at the GB due to the segregation of embrittling species; and (c) the energetics related to decohesion at the GB. The details are discussed below.

Segregation energetics for oxygen atoms at the grain boundary

To investigate the energetics related to the segregation of oxygen atoms at the GB, the energetics of oxygen atoms in bulk Ni are first investigated by computing the energy of an oxygen impurity in the substitutional site (S_b), in an octahedral interstitial site (I_O^O), and in a tetrahedral interstitial site (I_O^T). The oxygen formation energy is first calculated as

$$E_f = E_{\text{tot}}^{\text{O}} - E_{\text{tot}} - E_{\text{O}}. \quad (4)$$

Here, $E_{\text{tot}}^{\text{O}}$ is the total energy of system with oxygen impurity, E_{tot} the total energy of the clean system without oxygen, and E_{O} the total energy of one oxygen atom in an oxygen molecule (half of the total energy of oxygen molecule). A lower value of E_f implies more favorable oxygen binding tendency. The computed values of formation energy for oxygen at the various sites are listed in Table 5. It can be seen from these values that the oxygen impurity atom has the lowest energy in the octahedral site. This lower energy configuration for the oxygen impurity atoms is attributed to the larger free volume available at the octahedral site as compared to the tetrahedral site.

To investigate the effect of GB structure on the segregation behavior of oxygen atoms, the binding energy of the oxygen atom is calculated at various possible sites for the model GB systems. The sites for the occupancy of oxygen atoms considered here are (a) interstitial atomic sites at GB_0 layer (as identified in Fig. 2) with up to 4 oxygen atoms occupying the sites corresponding to a coverage of 0.25 ML (1 atom), 0.5 ML (2 atoms), 0.75 ML (3 atoms), and 1 ML (4 atoms) and (b) single oxygen atom at substitutional atomic sites from GB_0 up to GB_3 layer. It is expected that substitutional sites beyond GB_3 layers will not significantly affect the vacancy formation energy due to the distance from the GB plane. The computed values of the binding energy for oxygen atoms at various interstitial and substitutional sites

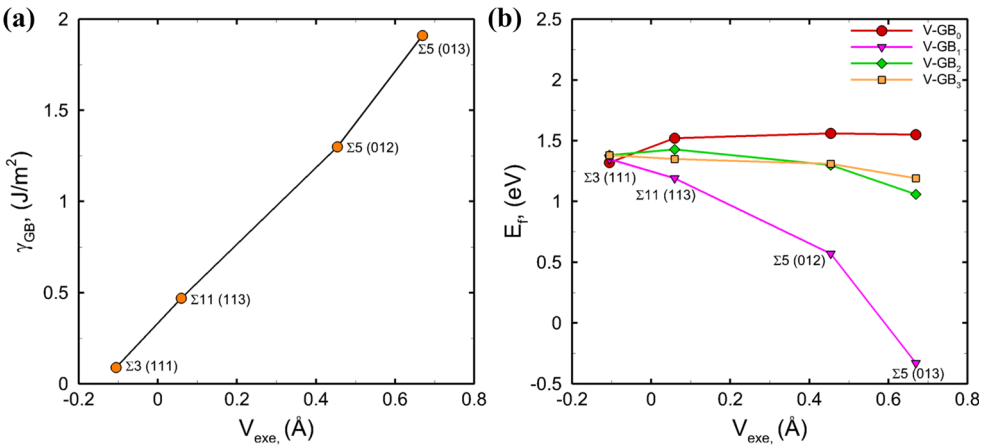

Figure 4 Plots showing the variation of **a** the GB energy and **b** vacancy formation energy as a function of the excess free volume.

Table 5 Calculated oxygen formation energy (eV) at tetrahedral (I_O^T), octahedral (I_O^O), and substitutional (S_b) site in bulk Ni

Site	E_f
I_O^T	0.11
I_O^O	−0.12
S_b	1.08

Table 6 Oxygen binding energy (eV) at various interstitial and substitutional sites close to GB

GB	Σ3 (111)	Σ5 (012)	Σ5 (013)	Σ11 (113)
I_1-GB_0	−0.32	−1.04	−1.33	−0.69
I_2-GB_0	−0.68	−1.08	−1.34	−0.62
I_3-GB_0	−0.81	−1.30	−1.86	−0.66
I_4-GB_0	−0.77	−1.34	−1.88	−0.66
S_1-GB_0	1.05	−0.14	−0.43	0.45
S_1-GB_1	1.10	−0.93	−1.75	−0.32
S_1-GB_2	1.13	−0.45	−0.13	−0.18
S_1-GB_3	1.13	−0.16	−0.17	0.16

Here, I_1-GB_0, I_2-GB_0, I_3-GB_0, and I_4-GB_0 correspond to 1, 2, 3, and 4 oxygen atoms at interstitial site along GB_0 layer, whereas S_1-GB_0, S_1-GB_1, S_1-GB_2, and S_1-GB_3 correspond to a single oxygen atom at substitutional site in GB_0, GB_1, GB_2, and GB_3 layers

close to GB are listed in Table 6 and plotted in Fig. 5. For the case of interstitial sites, it can be seen that oxygen binding is more favorable at the GB interstitial site as compared to the bulk octahedral site for all coverages considered. In particular, a strong binding preference is observed for the Σ5 (012) GB and Σ5 (013) GB, wherein the difference in binding energy is greater than 1 eV/atom. For the case of substitutional sites, Σ3 (111) GB shows a slightly lower binding energy (more favorable) at a low concentration. This value, however, is observed to increase with increased oxygen coverage making the GB substitutional sites less favorable than the bulk substitutional sites. The Σ5 (012) GB, the Σ5 (013) GB, and the Σ11 (113) GB all suggest lower binding energies (more favorable) than bulk substitutional sites for all coverages. For these GBs, the binding is observed to be most favorable at the GB_1 substitutional site as compared to the other layers. In comparison with all the cases considered, the oxygen binding at the interstitial site is much more favorable than the substitutional site as well as the bulk site. Thus, it can be seen that the Σ3 (111) CTB is the most resistant to oxygen segregation of the four GBs studied here and is attributed to the lowest V_{exe}.

DFT calculations are then carried out to investigate the effect of concentration of segregated oxygen on the vacancy formation energy. Based on the calculations in the previous section, substitutional sites at GB_1 and GB_2 corresponding to a lower vacancy formation energy are chosen to investigate this effect. The calculated values for vacancy formation energy at atomic site in these two layers with and without the presence of 1 ML oxygen atoms at the interstitial sites (all four sites) in the GB_0 layer are listed for comparison in Table 4. It can be seen from the values that the presence of oxygen segregated at the GB

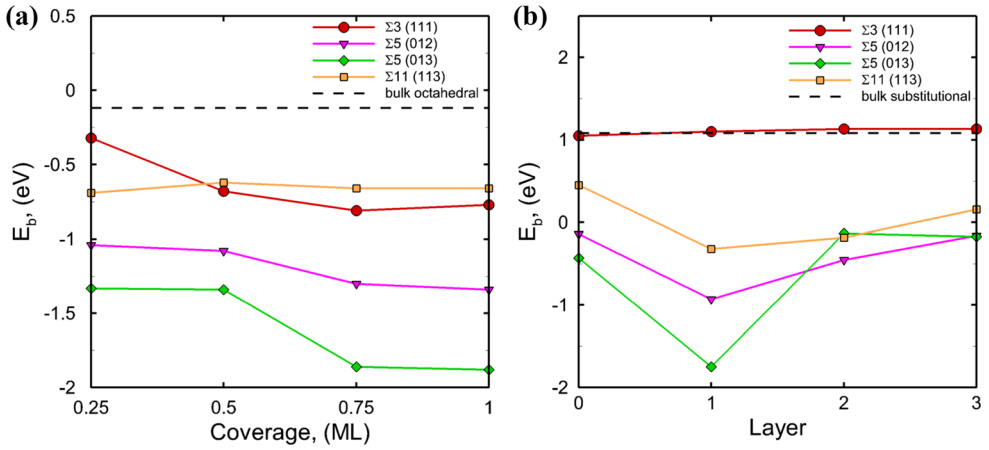

Figure 5 Plots showing **a** the variation of oxygen binding energy (per oxygen atom) at interstitial site as a function of oxygen coverage in GB_0 layer and **b** the variation of binding energy of a single oxygen atom at substitutional site up to GB_3 layer. *Gray dashed lines* correspond to oxygen binding energy of interstitial (octahedral) site for (**a**) and substitutional site for (**b**) in bulk system.

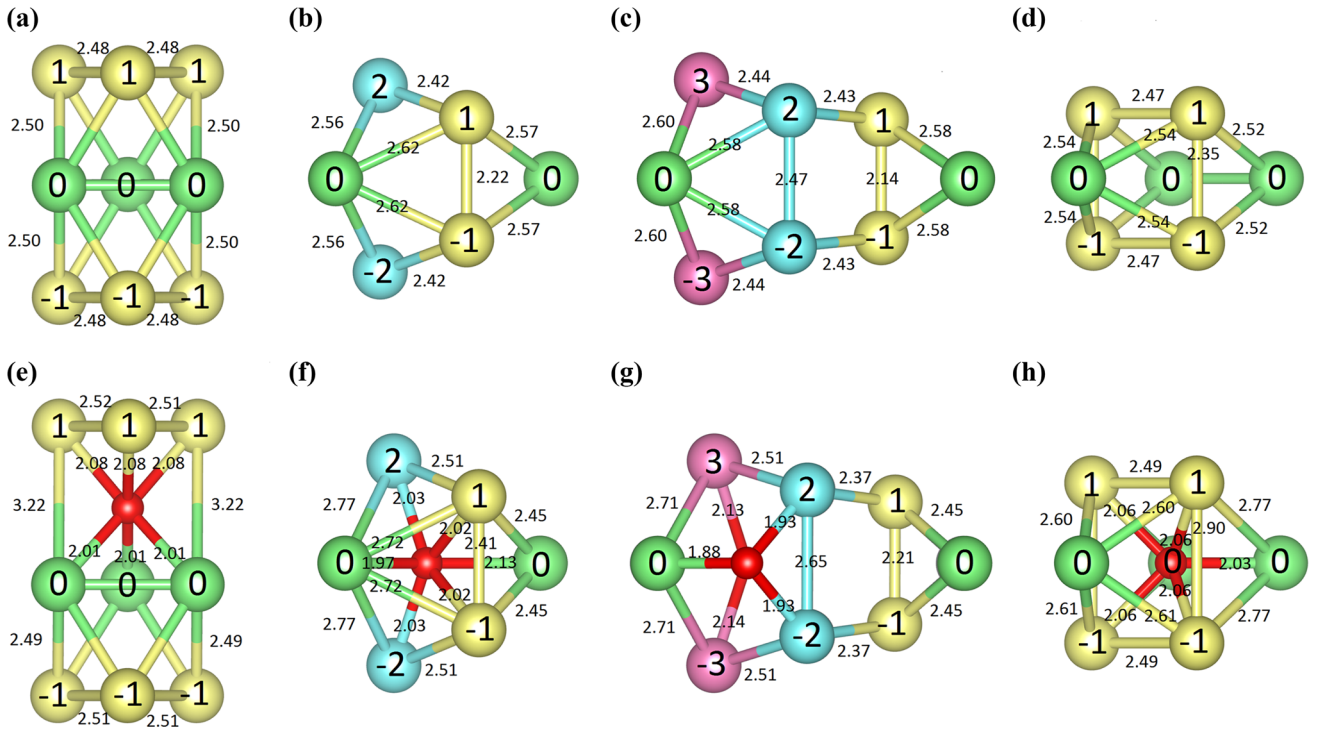

Figure 6 Calculated nearest-neighbor interatomic distances for clean GBs: **a** Σ3 (111), **b** Σ5 (012), **c** Σ5 (013) GB, and **d** Σ11 (113) GB. The modifications in the bonding environment and bond distances in the presence of segregated oxygen atom for **e** Σ3 (111), **f** Σ5 (012), **g** Σ5 (013), and **h** Σ11 (113) GBs.

results in more favorable vacancy formation for the Σ3 (111), Σ5 (012), and Σ11 (113) GBs. For the case of the Σ5 (013) GB, the segregation of oxygen results in less favorable vacancy formation for the GB_1 layer and more favorable vacancy formation for the GB_2 layer. This lowering of vacancy formation energy promotes the creation of vacancies at the GB and diffusion of the embrittling atoms to the GB and furthermore results in an increased concentration of the embrittling atoms at the GB. It is observed that while the Σ3 (111) GB has the lowest tendency to segregate oxygen atoms, oxygen segregation at the GB results in favorable formation of a vacancy in the GB_1 layer for the CTB that is likely to promote diffusion and trapping of more oxygen atoms at sites close to the GB.

The embrittling effect due to interstitial oxygen segregation can also be understood based on the modification in the bonding environment due to the segregation at the GB. The bonding environment at the oxygen segregation site for the four GBs is shown in Fig. 6 for the clean GB as well as for the system with 1 ML oxygen atom occupying interstitial site along with the various interatomic distances. It can be seen that the oxygen atoms are 5-coordinated for Σ5 (013) GB and 6-coordinated for all the other GBs. A slight increase in the Ni–Ni bond lengths at the GBs is observed due to the interstitial oxygen. The segregation of oxygen also affects the valence charge density distribution for the Ni atoms, as shown in Fig. 7. Also, the charge density is observed to be much higher between the oxygen atom and its neighboring Ni atoms than that between two Ni atoms for each GB, implying the formation of strong Ni–O bonds and weakening of the Ni–Ni bonds. To examine this effect in more detail, Bader charge analysis is employed to study the changes in the valence charge (net charge) induced by oxygen segregation along the GB. Table 7 lists the average net charge on the oxygen atoms and the binding Ni atoms at GB_0 layer for Σ3 (111) GB. It can be seen from these values that the presence of oxygen atoms leads to a substantial decrease in the net charge for the surrounding Ni atoms, especially with an increased number of oxygen atoms. This weakening of the Ni–Ni bonds due to the segregation of oxygen is likely to break the Ni–Ni bonds and result in the formation of cracks at the GB. The decohesion of GB due to the presence of segregated oxygen under tensile loading conditions is discussed below.

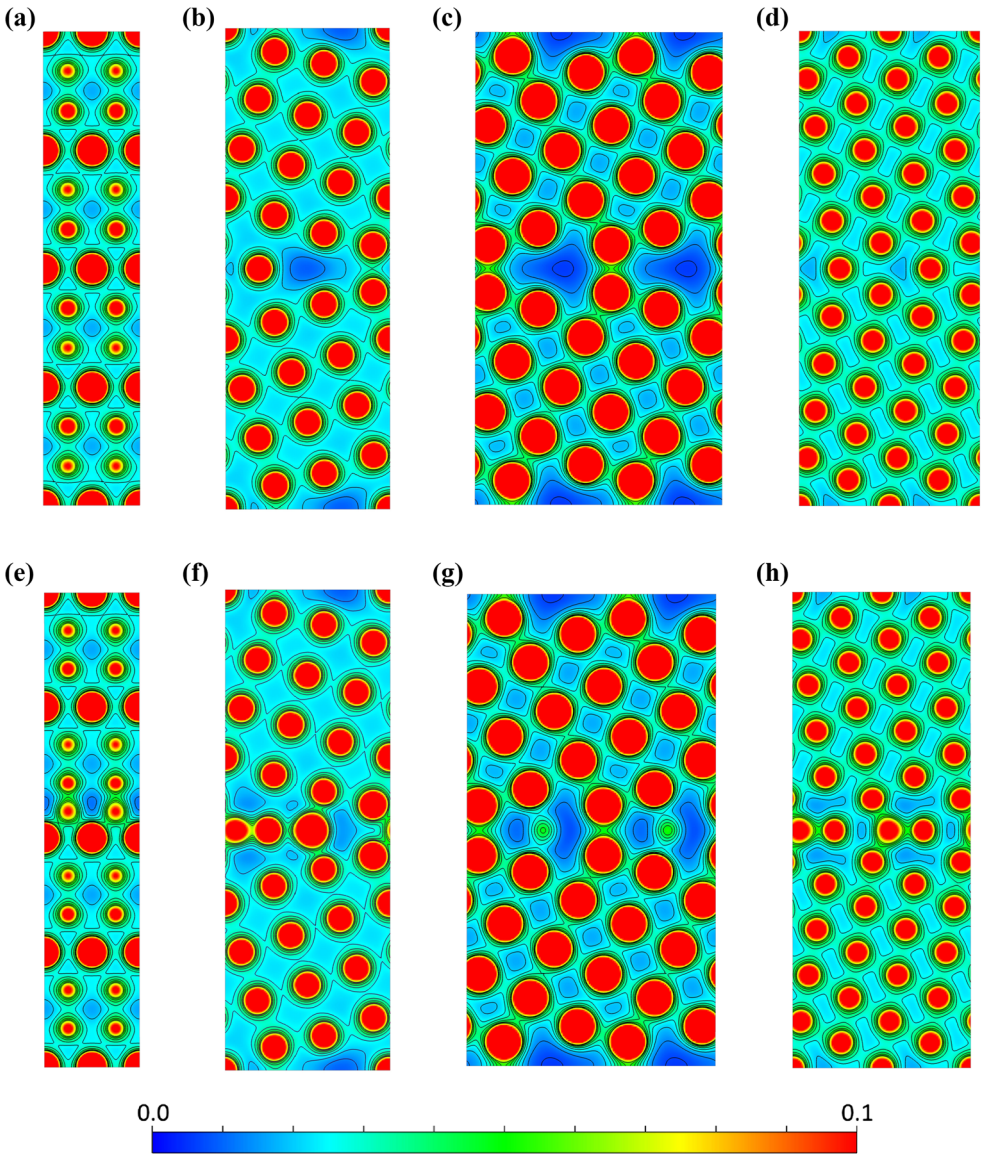

Figure 7 Side view of the calculated valence charge density distribution (electron/Bohr^3) for clean GBs: **a** Σ3 (111), **b** Σ5 (012), **c** Σ5 (013), and **d** Σ11 (113) GBs. The modified charge density in the presence of segregated oxygen for **e** Σ3 (111), **f** Σ5 (012), **g** Σ5 (013), and **h** Σ11 (113) GBs.

Table 7 Variation of net charge for oxygen and nickel (GB_0) for varying oxygen coverage at interstitial site in Σ3 (111) GB_0 layer

Coverage (ML)	0.25	0.5	0.75	1
Q_{Ni}	0.20	0.29	0.42	0.54
Q_O	−1.21	−1.14	−1.08	−1.01

Table 8 W_s (J/m^2) for varying oxygen coverage at interstitial site in GB_0 layer

Coverage (ML)	0	0.25	0.5	0.75	1
Σ3 (111)	1.86	0.93	0.63	0.70	1.11
Σ5 (012)	1.75	1.46	1.19	1.01	0.79
Σ5 (013)	1.43	1.24	1.06	1.05	0.95
Σ11 (113)	2.04	1.62	1.39	1.00	0.81

Oxygen segregation-induced GB decohesion

The tendency to form a crack at the oxygen-segregated GBs can be understood by computing the energy required to pull the system apart at a desired fracture plane, i.e., the work of separation W_s [65]. W_s is calculated as the work required to cleave a GB into free surfaces, as given by the following equation:

$$\gamma^{GB} = E_{FS} - \frac{E_{GB}}{2}, \quad (5)$$

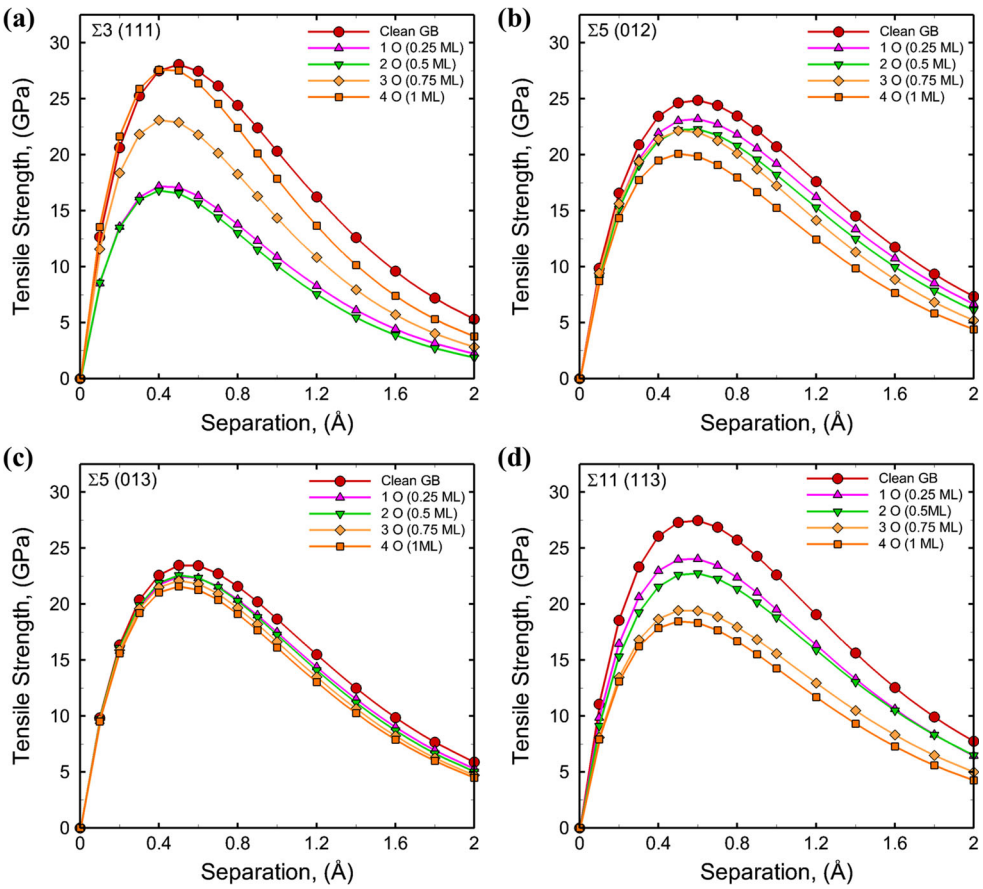

Figure 8 Predicted tensile strength as a function of separation distance for the **a** Σ3 (111) GB, **b** the Σ5 (012) GB, **c** the Σ5 (013) GB, and **d** the Σ11 (113) GB as a function of oxygen concentration (1–4 oxygen atoms in GB_0 layer) in comparison with that for the clean GB.

where E_{FS} is the free surface energy per unit area, calculated similarly to E_{GB} as defined before. The calculated value for E_{FS} of 2.40 J/m^2 for the clean Σ5 (012) GB is in reasonable agreement with the reported values of 2.65 J/m^2 [30], 2.34 J/m^2 [31], and 2.21 J/m^2 [32] in the literature. The work of separation is computed for the clean GB systems and the GB systems with segregated oxygen atoms to investigate the effects of the segregated oxygen on the energetics of crack formation. Various planes of separation are considered for the GB systems and the GB_0–GB_1 plane (between the two layers) is found to have the lowest W_s for all the GBs. This GB_0–GB_1 plane is therefore considered to be the weakest plane, i.e., the GB decohesion plane. The computed values of W_s for this decohesion plane are listed in Table 8 for all the GBs with and without the segregated oxygen. The values indicate that W_s is lower in the presence of segregated oxygen at the GB for all the GBs considered. Notably, W_s is observed to decrease with increasing coverage of segregated oxygen for the Σ5 (012), Σ5 (013), and Σ11 (113) GBs up to 1 ML. This drop in W_s indicates a strong decohesion effect induced by oxygen, since a smaller W_s implies that, in the presence of oxygen along the GB, less energy is now required for the GB to be pulled apart along the GB_0–GB_1 plane. This decrease in W_s with oxygen segregation is found to be the most significant for the Σ11 (113) GB. The largest decrease in W_s for the Σ3 (111) GB is found to occur at a coverage of 2 oxygen atoms (0.5 ML), indicating that with a certain amount of segregated oxygen atoms at the GBs, the Σ3 (111) CTB has the highest possibility to form a crack. A higher concentration of oxygen renders slightly higher W_s values but the values are less than those for clean GBs. A comparison of the values of W_s for all the GBs considered suggests the lowest values for the Σ11 (113) GB at the lowest concentration of segregated oxygen. These results therefore suggest the highest tendency to form a crack due to the presence of segregated oxygen.

Furthermore, a rigid separation test is performed to examine the response of the GB under tensile loading, where two grains are incrementally separated along GB_0–GB_1 plane in GB normal direction, with atom positions fixed. The separation increment is set

Table 9 Maximum tensile strength σ_{max} (GPa) for varying oxygen coverage at interstitial site in GB_0 layer

Coverage (ML)	0	0.25	0.5	0.75	1
Σ3 (111)	28.06	17.24	16.83	23.25	28.10
Σ5 (012)	24.89	23.23	22.35	22.10	20.09
Σ5 (013)	23.55	22.51	22.60	22.11	21.59
Σ11 (113)	27.51	24.12	22.79	19.51	18.49

Table 10 Hydrogen binding energy (E_b) for varying hydrogen coverage at interstitial site in Σ3 (111) GB_0 layer

Coverage (ML)	0.25	0.5	0.75	1
E_b (eV)	0.60	0.59	0.62	0.70
Bulk	0.02(I_O^O)			

Bulk interstitial results for octahedral (I_O^O) site are also listed for comparison

to be 0.1 Å till 1 Å and 0.2 Å beyond, up to 2 Å. The energy increase per unit area is fitted to the Rose universal binding curve (UBC) [66] written as

$$f(x) = 2\gamma - 2\gamma\left(1 + \frac{x}{\lambda}\right)\exp\left(-\frac{x}{\lambda}\right). \quad (6)$$

The derivative of the UBC curve is used to plot the variation of the tensile stress as a function of increasing separation distance as shown in Fig. 8. The values computed for the peak tensile stress (σ_{max}) for the various clean GB systems as well as GB systems with varying oxygen concentrations are listed in Table 9. The values for the peak tensile stress with the concentration of segregated oxygen indicate similar trends suggested by the work of separation, where the most significant decrease is observed for the Σ3 (111) GB at a coverage of 2 oxygen atoms at the GB (0.5 ML).

These results suggest that the segregation of oxygen at the GBs substantially decreases the critical stress for crack formation and maximum tensile strength of the GB for all the Ni GBs considered. In particular, this decohesion effect is observed to be the strongest for the Σ3 (111) CTB that shows the highest susceptibility to form cracks in the presence of segregated oxygen atoms. These CTBs, however, are found to be more resistant to oxygen segregation and beneficial in the design of materials' microstructures. Thus, a contradictory role of Σ3 (111) CTB is observed toward the strengthening of Ni microstructures in environments exposed to oxygen at high temperatures.

Decohesion of Ni GBs due to hydrogen segregation

To further explore the contradictory role of the Σ3 (111) CTB in embrittlement of Ni, the study is extended to examine the decohesion of Ni due to segregation of hydrogen at the GBs. The decohesion effect is investigated using the same model GB systems and examining the effect of segregation of hydrogen at the GB on the work of separation for varying hydrogen concentrations at the GB. The hydrogen binding energy is first calculated as a function of coverage (0.25, 0.5, 0.75, and 1 ML) for the Σ3 (111) CTB and the values are listed in Table 10. The calculations suggest that the hydrogen binding at the interstitial site in GB_0 layer is found to be less favorable as compared to the bulk octahedral site for all the coverages considered, in contrary to oxygen, which prefers interstitial sites at the GB_0 layer. Thus, the hydrogen atoms prefer to be in the bulk as compared to the Σ3 (111) CTB suggesting that the presence of Σ3 (111) CTBs renders high resistance to hydrogen segregation.

To investigate this further, the work of separation W_s is calculated for the Σ3 (111) CTB as a function of coverage of hydrogen atoms at the GB_0 layer for the Σ3 (111) CTB and the values are listed in Table 11. It can be seen that W_s shows a consistent decrease with an increase in hydrogen concentration up to 1 ML, reaching a value very close to 0 at full coverage, suggesting a catastrophic decohesion effect due to hydrogen segregation. This is different from the case for oxygen segregation, which presents the most pronounced decohesion at 0.5 ML. Therefore, the decohesion effect of hydrogen at Σ3 (111) CTB is more significant than oxygen.

To compare this behavior with the other GBs, W_s is further calculated for the other GBs in the presence of four segregated hydrogen atoms (1 ML) at the GB_0 layer and the obtained values are listed in Table 12. For the Σ5 (012) GB, the Σ5 (013) GB, and the Σ11 (113) GB, the decrease in W_s is less significant as compared to the case for oxygen segregation, indicating that hydrogen causes less decohesion effect for these GBs as compared to oxygen. In comparison, with a low W_s, Σ3 (111) CTB is the most susceptible to crack formation in the presence of segregated hydrogen atoms. The decrease in W_s for segregated hydrogen is observed to be more significant than that for segregated oxygen. These results agree with the

Table 11 W_s (J/m^2) for varying hydrogen coverage at interstitial site in Σ3 (111) GB_0 layer

Coverage (ML)	0	0.25	0.5	0.75	1
W_s (J/m^2)	1.86	1.44	1.02	0.57	0.01

Table 12 W_s (J/m^2) for 1 ML hydrogen coverage at interstitial site in GB_0 layer

GB	Σ3 (111)	Σ5 (012)	Σ5 (013)	Σ11 (113)
Clean GB	1.86	1.75	1.43	2.04
4 H (1 ML)	0.01	1.50	1.32	1.63

Table 13 Variation of net charge for hydrogen and nickel (GB_0) for varying hydrogen coverage at interstitial site in Σ3 (111) GB_0 layer

Coverage (ML)	0.25	0.5	0.75	1
Q_{Ni}	0.06	0.11	0.17	0.29
Q_H	−0.31	−0.34	−0.33	−0.36

recent experimental results that suggest that the Σ3 CTBs are most susceptible to crack initiation due to decohesion [42]. Such decohesion attributed to hydrogen segregation is also likely to be induced by its effect on vacancy formation and superabundant vacancy formation in NiH [67]. Moreover, the average net charge as listed in Table 13 shows that the net charge of Ni atom is lower than that calculated in the presence of oxygen atoms.

Thus, the Σ3 (111) CTB is found to have the greatest decohesion effect and least resistant to crack initiation in the presence of segregated hydrogen as compared to the other GBs considered here. The Σ3 (111) CTB is therefore the most susceptible to decohesion in the presence of oxygen and even more so for hydrogen.

Conclusions

The energetics related to oxygen and hydrogen segregation-induced embrittlement of polycrystalline Ni is investigated using density functional theory calculations. A strong correlation among GB energy, oxygen binding energy, vacancy formation energy, and GB excess free volume is established, which implies that a more open structure results in a higher GB energy and is more prone to oxygen and vacancy segregation. The DFT calculations suggest that for the case of oxygen as the embrittling species, the oxygen binding at the GB interstitial site is much more favorable than the octahedral site in the bulk, indicating a preferred segregation at the GB. The presence of segregated oxygen facilitates vacancy formation at sites close to the GB, which promotes diffusion of the embrittling atoms to the GB and is expected to result in an increased concentration of the embrittling atoms at the GB. The segregation of oxygen at the GB leads to a substantial decrease in the work of separation at the GB, i.e., an increased tendency to form cracks. This GB decohesion effect is observed to be most significant for the Σ3 (111) CTB, which shows the least preference for oxygen segregation as compared to the other GBs considered. This contradictory role of the Σ3 (111) CTB is also investigated for the case of hydrogen as the embrittling species. For the case of hydrogen, the binding at the octahedral site in the bulk is observed to be more preferential than that at the GB interstitial site, indicating a much higher resistance to hydrogen segregation at the GB. However, an even more substantial GB decohesion effect and crack formation tendency are observed in the presence of small amounts of segregated hydrogen as compared to oxygen. Thus, while the CTB can provide enhanced mechanical strength for the Ni-based microstructures and higher segregation resistance for oxygen and hydrogen, it offers least resistance to crack nucleation in the presence of very small amounts of segregated oxygen or hydrogen. This decohesion response of the Σ3 (111) CTB in the presence of embrittling species can be challenging in the design of nickel-based microstructures with a high density of Σ3 (111) CTB.

Acknowledgements

This material is based upon work supported by the National Science Foundation (NSF) CMMI Grant-1454547.

References

[1] Pang XJ, Dwyer DJ, Gao M, Valerio P, Wei RP (1994) Surface enrichment and grain boundary segregation of niobium in Inconel 718 single and poly-crystals. Scr Metall et Mater 31:345–350

[2] Fournier L, Delafosse D, Magnin T (2001) Oxidation induced intergranular cracking and Portevin-Le Chatelier effect in nickel base superalloy 718. Mater Sci Eng A 316:166–173

[3] Carpenter W, Kang BS-J, Chang MK (1997) SAGBO Mechanism on high temperature cracking behavior of Ni-base superalloys, Proceeding of the. Superalloys 718, 625, 706, and Various Derivatives, Pittsburgh, p 679

[4] Smith DF, Smith JS, Russell KC, Smith DF (eds) (1990) Physical metallurgy of controlled expansion invar-type alloys. TMS, Warrendale, p 253

[5] Browning PF, Henry MF, Rajan K, Loria EA (eds) (1997) Superalloys 718, 625, 706 and various derivatives. TMS, Warrendale, p 665

[6] Rösler J, Müller S (1998) Protection of Ni-based superalloys against stress accelerated grain boundary oxidation (SAGBO) by grain boundary oxidation by grain boundary chemistry modification. Scripta Mater 40:257–263

[7] Bricknell H, Woodford DA (1981) The embrittlement of nickel following high temperature air exposure. Metall Trans A 12:425–433

[8] Woodford DA (1981) Environmental damage of a cast nickel base superalloy. Metall Trans A 12:299–308

[9] Pfaendtner JA, McMahon CJ Jr (2001) Oxygen-induced intergranular cracking of a Ni-base alloy at elevated temperatures—an example of dynamic embrittlement. Acta Mater 49:3369–3377

[10] Rezende MC, Araújo LS, Gabriel SB, Dille J, De Almeida LH (2015) Oxidation assisted intergranular cracking under loading at dynamic strain aging temperatures in Inconel 718 superalloy. J Alloys Compd 643:S256–S259

[11] Krupp U (2005) Dynamic Embrittlement—time–dependent quasi–brittle intergranular fracture at high temperatures. Int Mater Rev 50:83–97

[12] Krupp U, Wagenhuber P, Kane WM et al (2005) Environmentally assisted brittle fracture of nickel-base superalloys at high temperatures, 11th international conference on fracture. ICF11, 01

[13] Perusin S, Monceau D, Andrieu E (2005) Investigations on the diffusion of oxygen in nickel at 1000 °C by SIMS analysis. J Electrochem Soc 152(12):E390–E397

[14] Jiang DE, Carter EA (2004) First principles assessment of ideal fracture energies of materials with mobile impurities: implications for hydrogen embrittlement of metals. Acta Mater 52:4801–4807

[15] Pundt A, Kirchheim R (2006) Hydrogen in metals: microstructural aspects. Annu Rev Mater Res 36:555–608

[16] Matsumoto R, Taketomi S, Matsumoto S, Miyazaki N (2009) Atomistic simulations of hydrogen embrittlement. Int J Hydrog Energy 34:9576–9584

[17] Oudriss A, Creus J, Bouhattate J et al (2012) Grain size and grain-boundary effects on diffusion and trapping of hydrogen in pure nickel. Acta Mater 60:6814–6828

[18] Angelo JE, Moody NR, Baskes MI (1995) Trapping of hydrogen to lattice defects in nickel. Model Simul Mater Sci Eng 3:289–307

[19] Yamaguchi M, Shiga M, Kaburaki H (2004) First-principles study on segregation energy and embrittling potency of hydrogen in Ni Σ5 (012) tilt grain boundary. J Phys Soc Jpn 73:441–449

[20] Kart HH, Cagin T (2008) The effects of boron impurity atoms on nickel Σ5 (012) grain boundary by first principles calculations. J Achiev Mater Manuf Eng 30:177–181

[21] Siegel DJ, Hamilton JC (2005) Computational study of carbon segregation and diffusion within a nickel grain boundary. Acta Mater 53:87–96

[22] Yamaguchi M, Shiga M, Kaburaki H (2005) Grain boundary decohesion by impurity segregation in a nickel-sulfur System. Science 21:307–397

[23] Schusteritsch G, Kaxiras E (2012) Sulfur-induced embrittlement of nickel: a first-principles study. Model Simul Mater Sci Eng 20:065007

[24] Yamaguchi M, Shiga M, Kaburaki H (2006) Grain boundary decohesion by sulfur segregation in ferromagnetic iron and nickel—a first-principles study. Mater Trans 47:2682–2689

[25] Kart HH, Uludogan M, Cagin T (2009) DFT studies of sulfur induced stress corrosion cracking in nickel. Comput Mater Sci 44:1236–1242

[26] Chen L, Peng P, Zhuang HL, Zhou DW (2006) First-principle investigation of bismuth segregation at Σ5 (012) grain-boundaries in nickel. Trans Nonferrous Met Soc China 16:813–819

[27] Gao Q, Widom M (2014) First-principles study of bismuth films at transition-metal grain boundaries. Phys Rev B 90:144102

[28] Bentria ELT, Lefkaier IK, Bentria B (2013) The effect of vanadium impurity on Nickel Σ5 (012) grain boundary. Mater Sci Eng A 577:197–201

[29] Liu WG, Han H, Ren CL et al (2014) First-principles study of intergranular embrittlement induced by Te in the Ni Σ5 grain boundary. Comput Mater Sci 88:22–27

[30] Yamaguchi M, Shiga M, Kaburaki H (2004) Energetics of segregation and embrittling potency for non-transition elements in the Ni Σ5 (012) symmetrical tilt grain boundary: a first-principles study. J Phys 16:3933–3955

[31] Vsianska M, Sob M (2011) The effect of segregated sp-impurities on grain boundary and surface structure, magnetism and embrittlement in nickel. Prog Mater Sci 56:817–840

[32] Razumovskiy VI, Lozovoi AY, Razumovskii IM (2015) First-principles-aided design of a new Ni-base superalloy: influence of transition metal alloying elements on grain boundary and bulk cohesion. Acta Mater 82:369–377

[33] Liu W, Han H, Ren C, Yin H, Zou Y, Huai P, Xu H (2015) Effects of rare-earth on the cohesion of Ni Σ 5(012) grain boundary from first-principles calculations. Comput Mater Sci 96:374–378

[34] Krupp U, Kane W, Pfaendtner JA et al (2004) Oxygen-induced intergranular fracture of the nickel-base alloy IN718 during mechanical loading at high temperatures. Mater Res 7:35–41

[35] Yang SL, Krupp U, Christ HJ, Trindade VB (2005) The relationship between grain boundary character and the intergranular oxide distributionin IN718 superalloy. Adv Eng Mater 7(8):723–726

[36] Palumbo G, Aust KT (1995) Solute effects in grain boundary engineering. Can Metall Quart 34:165–173

[37] Watanabe T (1994) The impact of grain boundary character distribution on fracture in polycrystals. Mat Sci Eng A 176:39–49

[38] Bechtle S, Kumar M, Somerday BP, Launey ME, Ritchie RO (2009) Grain-boundary engineering markedly reduces susceptibility to intergranular hydrogen embrittlement in metallic materials. Acta Mater 57:4148–4157

[39] Stefano DD, Mrovec M, Elsässe C (2015) First-principles investigation of hydrogen trapping and diffusion at grain boundaries in nickel. Acta Mater 98:306–312

[40] Alvaro A, Jensen IT, Kheradmand N, Løvvik OM, Olden V (2015) Hydrogen embrittlement in nickel, visited by first principles modeling, cohesive zone simulation and nanomechanical testing. Int J Hydrog Energy 40:16892–16900

[41] Barrowsa Wesley, Dingreville Rémi, Spearot Douglas (2016) Traction–separation relationships for hydrogen induced grain boundary embrittlement in nickel via molecular dynamics simulations. Mater Sci Eng, A 650:354–364

[42] Seita M, Hanson JP, Gradecak S et al (2015) The dual role of coherent twin boundaries in hydrogen embrittlement. Nat Commun 6:6164

[43] Creuze J, Berthier F, Tétot R (2001) Wetting and structural transition induced by segregation at grain boundaries: a Monte Carlo study. Phys Rev Lett 86:5735–5738

[44] Frolov T, Olmsted DL, Asta M, Mishin Y (2013) Structural phase transformations in metallic grain boundaries. Nat Commun 4:1899

[45] Frolov T, Asta M, Mishin Y (2015) Segregation-induced phase transformations in grain boundaries. Phys Rev B 92:020103(R)

[46] Sangid MD, Sehitoglu H, Maier HJ, Niendorf T (2010) Grain boundary characterization and energetics of superalloys. Mater Sci Eng, A 527:7115–7125

[47] Duparc OH, Poulat S, Larere A, Thibault J, Priester L (2000) High-resolution transmission electron microscopy observations and atomic simulations of the structures of exact and near $\Sigma = 11$, 332 tilt grain boundaries in nickel. Philos Mag A 80(4):853–870

[48] Kresse G, Furthmüller J (1996) Efficiency of ab-initio total energy calculations for metals and semiconductors using a plane-wave basis set. Comput Mater Sci 6:15–50

[49] Kresse G, Furthmuller J (1996) Efficient iterative schemes for ab initio total-energy calculations using a plane-wave basis set. Phys Rev B 54:11169–11186

[50] Blochl PE (1994) Projector augmented-wave method. Phys Rev B 50:17953–17979

[51] Kresse G, Joubert D (1999) From ultrasoft pseudopotentials to the projector augmented-wave method. Phys Rev B 59:1758–1775

[52] Perdew JP, Burke K, Ernzerhof M (1996) Generalized gradient approximation made simple. Phys Rev Lett 77:3865–3868

[53] Monkhorst HJ, Pack JD (1976) Special points for Brillouin-zone integrations. Phys Rev B 13:5188–5192

[54] Čák M, Šob M, Hafner J (2008) First-principles study of magnetism at grain boundaries in iron and nickel. Phys Rev B 78:054418

[55] Cho JH, Zhang ZY, Plummer EW (1999) Oscillatory lattice relaxation at metal surfaces. Phys Rev B 59:1677–1680

[56] Steyskal EM, Oberdorfer B, Sprengel W (2012) Direct experimental determination of grain boundary excess volume in metals. Phys Rev Lett 108:055504

[57] Olmsted DL, Foiles SM, Holm EA (2009) Survey of computed grain boundary properties in face-centered cubic metals: I. grain boundary energy. Acta Mater 57:3694–3703

[58] Mehrer H (2007) Diffusion in solids. Springer, New York

[59] Seeger A, Schottky G (1959) Energy and electrical resistivity of high-angle grain boundaries in metals. Acta Metall 7:495–505

[60] Zhang H, Srolovitz DJ (2006) Simulation and analysis of the migration mechanism of R5 tilt grain boundaries in an fcc metal. Acta Mater 54:623–633

[61] Shiga M, Yamaguchi M, Kaburaki H (2003) Structure and energetics of clean and hydrogenated Ni surfaces and symmetrical tilt grain boundaries using the embedded-atom method. Phys Rev B 68:245402

[62] Coleman SP, Spearot DE, Capolungo L (2013) Virtual diffraction analysis of Ni [0 1 0] symmetric tilt grain boundaries. Modell Simul Mater Sci Eng. 21:055020

[63] Korhonen T, Puska MJ, Nieminen RM (1995) Vacancy-formation energies for fcc and bcc transition metals. Phys Rev B 51:9526–9532

[64] Smedskjaer LC, Fluss MJ, Legnini DG, Chason MK, Siegel RW (1981) The vacancy formation enthalpy in Ni determined by positron annihilation. J Phys F 11:2221

[65] Hashibon A, Elsässer C, Mishin Y, Gumbsch P (2007) First-principles study of thermodynamical and mechanical stabilities of thin copper film on tantalum. Phys Rev B 76:245434

[66] Rose JH, Ferrante J, Smith JR (1981) Universal binding energy curves for metals and bimetallic interfaces. Phys Rev Lett 47:675–678

[67] Zhang C, Alavi A (2005) First-principles study of superabundant vacancy formation in metal hydrides. J Am Chem Soc 127:9808–9817